

## FLUORESCENT PIV TECHNIQUE FOR TURBOMACHINERY FLOWS

M. Okada, J. Pinho, B. Cernat, S. Lavagnoli  
Turbomachinery and Propulsion Department, von Karman Institute for Fluid dynamics, Belgium

### ABSTRACT

One of the major sources of concern for experimentalists employing Particle Image Velocimetry (PIV) is undesired strong light reflections on surfaces of channel walls or obstacles. The issue is emphasized in applications composed of complex geometries with highly reflective surfaces such as turbomachinery rigs. This paper presents the development and applications of the fluorescent PIV technique as a countermeasure for such a problem. Employment of fluorescent dye-doped tracer particles with a wavelength-specific optical filter enables the separation of the Stokes-shifted particle light emission from reflections on the surfaces.

Aiming at applying the technique to engine-like turbomachinery flows, the fluorescent tracer particles were made out of pyromethene 567 and Di-Ethyl-Hexyl-Sebacat considering multiple aspects of characteristics.

Two application cases are reported in this paper, firstly the developed particles were tested in a low-speed wind tunnel with a metal turbine blade placed in the flow path and a laser sheet oriented to impinge the blade surface. With the installation of an adequate optical filter, the undesired light reflections were successfully removed, and reasonable vector calculations were enabled in proximity to the reflective blade surfaces. Secondly, the fluorescent PIV was performed on a high-pressure turbine stage hosted in a high-speed short-duration rotating turbine rig to demonstrate the feasibility of the technique in engine-representative turbomachinery flows.

### NOMENCLATURE

$C_{ax}$	Axial chord of rotor
DEHS	Di-Ethyl-Hexyl-Sebacat
FWHM	Full-Width-at-Half-Maximum
HPT	High-pressure turbine
$L$	Extraction lines
$Mach_{03,rel}$	Relative Mach number at stage outlet
$\dot{m}_{purge}$	Purge mass flow rate
$\dot{m}_{total}$	Main mass flow rate
PIV	Particle image velocimetry
P567	Pyromethene 567

$P_{01}$	Total pressure at stage inlet [Pa]
$P_{s3}$	Static pressure at stage outlet [Pa]
RANS	Reynolds averaged Navier-Stokes simulation
$Re_{03,rel}$	Relative Reynolds number at stage outlet
$t$	Time
$x$	Axial distance

### INTRODUCTION

Particle Image Velocimetry (PIV) is a powerful measurement tool that can obtain instantaneous spatial flow data. However, in some cases such as turbomachinery test rigs which often contain reflective surfaces with complex geometries, undesired reflections on surfaces trouble experimentalists because vector calculations cannot be performed when particle images are overwhelmed by reflections. Furthermore, the incidence of excessively strong light in image sensors can cause permanent damage to pixels. To overcome such a challenge, the use of fluorescence dye-doped particles and optical filters was investigated to separate the fluorescent emission of particles from reflections.

In gas phase flows, tracer particles are generally required to be micron or sub-micron size to fulfill acceptable traceability. Moreover, a large quantity of tracer particles is required for seeding in wind tunnels, especially those with large-scale, high-speed, or open-looped systems. Lee & Nishida [1] used fluorescent particles for a two-phase flow aiming at velocity field measurements of large liquid phase droplets and surrounding gas simultaneously and independently. Tracers (6.3 - 8.5  $\mu\text{m}$  diameter) for the air motion were made of Rhodamine B - water solution and illuminated by a 532 nm wavelength Nd:YAG laser. An optical low-pass filter was used for fluorescence imaging. Similarly, Kosiwczuk et al. [2] investigated the use of fluorescent particles for two-phase flow, but both tracers for air motion and large droplets were dye-doped. Stilbene420 was dissolved in methanol and formed into 1-5  $\mu\text{m}$  droplets using a nebulizer to track the gas-phase flow. The particles were illuminated by a frequency tripled Nd:YAG laser (355 nm wavelength) and fluorescence emissions were separated by a set of optical filters. It is

assumed that the methanol-base fluorescent particles can be only used in room or low-temperature environments due to the low boiling point of methanol (64.7 °C). Chennaoui et al. [3] developed micron-sized Bis-MSB dye-doped o-xylene droplets which have high excitation efficiency in the UV light range. The dye performance in the droplets was evaluated quantitatively in a stable emulsion state and PIV was performed in a laboratory flow around a metal blade. Petrosky et al. [4] demonstrated PIV using Kiton Red 620 (KR620) doped submicron scale Polystyrene Latex microspheres in a free jet and a two-phase flow apparatus. A conventional 532 nm double pulsed Nd:YAG at 200 mJ/pulse intensity illuminated the flow and a 560 nm long pass optical filter blocked Mie scattered light and reflections. Bhattacharya et al. [5] performed PIV in a multistage research compressor using Rhodamine B 610 doped tracer particles based on propylene glycol including 1.3% by volume of ethanol to reduce the surface tension of the seeding fluid. A 532 nm Nd:YAG laser illuminated flow and a 540 nm long pass filter blocked undesired reflections.

In our study, aiming at applying the technique for experiments in engine-relevant turbomachinery flows, we set the requirement of the particle specification as follows: easy preparation for large quantity, sub-micron size, high fluorescent emission efficiency at 527 nm wavelength excitation (high-speed Nd: YLF laser system), feasibility to seeded large quantity economically, and high-temperature resistance (>500 K). The developed tracer particles were tested in a conventional low-speed wind tunnel and a high-speed short-duration turbine test rig to demonstrate the capability of the technique.

### FLUORESCENT TRACER PARTICLES

For the particle base, Di-Ethyl-Hexyl-Sebacat (DEHS) was selected as it is compatible with Laskin nozzle particle generator which can produce a large number of submicron droplets (approximately  $10^8$  particles / second according to the manual). Besides, it has a higher boiling point of 523 K compared to other candidates such as methanol or olive oil. Pyrromethene 567 (P567) was selected as a dye considering its high fluorescent quantum yield at 527 nm wavelength excitation and solubility in DEHS. In addition, it must be noted that the toxicity of materials is also an important aspect to be concerned with as seeded gas is inherently more difficult to contain in designated space than liquid. The hazardous level of P567 is essentially lower compared to commonly used Rhodamine dyes. Nevertheless, the authors emphasize that the product must be dealt with carefully, the proper protective measures such as ventilators, masks, and skin and eye protections should be properly employed.

Fig. 1 shows the fluorescence spectra of P567-doped DEHS at different concentrations measured using a spectrometer (*Ocean Optics HR4000*) under

a similar setup described in [2]. The dye solutions with different concentrations were contained in disposable polystyrene cuvettes (*BRAND 759030*) and excited by a high-speed dual cavity YLF laser system (*Quantronix Darwin-Duo*, 527 nm wavelength). A variation of spectrum profiles depending on dye concentrations was confirmed, and the emission peaks appeared in a range between 540 and 585 nm. Note that, this conventional spectroscopic measurement on bulky dye solutions contained in cuvettes does not represent the fluorescence emission on sub-micron scale droplets with corresponding dye concentration because of inner filter (self-absorption) [3] or self-quenching effect. Still, the acquired data can forecast the spectrum of fluorescence from sub-micron droplets, and thus helpful for determining proper optical filters. An OD6 optical band-stop filter that has a central wavelength of 532 nm with 10 nm Full-Width-at-Half-Maximum (FWHM) and a long-pass colored glass filter that has a cut-on wavelength at 550nm were tested to assess the filtering efficacy.

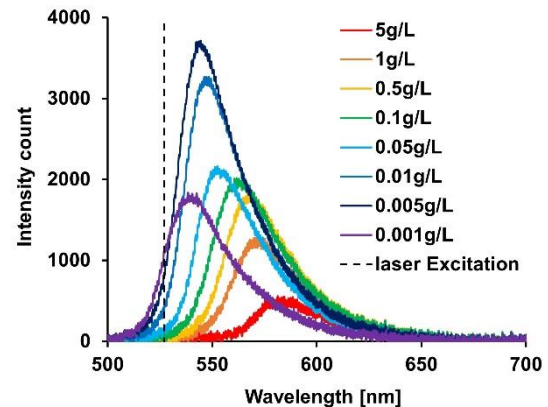


Fig. 1 Emission spectra of P567-doped DEHS bulk solution at different concentrations.

Suitable dye concentration in a form of sub-micron droplets for PIV measurements was assessed by comparing pixel intensities of raw fluorescence particle images captured in low-speed wind tunnel equipped with a backward-facing step. The mean flow speed was set to 5 m/s. Seven dye concentration solutions ranging from 0 g/L to 2.0 g/L were prepared and formed into sub-micron particles by PIVTEC PIVPart14 Laskin nozzle seeding generator. A high-speed Phantom M310 camera and a high-speed Nd:YLF (527 nm wavelength) Quantronix Darwin-Duo laser were used for shooting. The camera was equipped with a Nikon AF Micro-Nikkor 60mm f/2.8D lens. The optical band-stop filter (532 nm central wavelength, 10 nm FWHM) was attached to the lens.

Fig. 2 shows example snapshots of fluorescent particle images with concentrations of (A) 0.75 g/L and (B) 2.0 g/L. Fig. 3 presents the time- and area-averaged pixel intensity of fluorescent particle images at different dye concentrations. Within the measured range, the relation is almost linearly

proportional, implying the absence of a self-absorption effect at the demonstrated particle size and seeding density. Therefore, the optimum dye concentration is to be chosen considering the cost of materials, the solubility of the dye, the sensitivity of cameras, and the performance of optical filters. The demonstrations in this paper show practically achievable setups which can also be fitting for a wide range of applications.

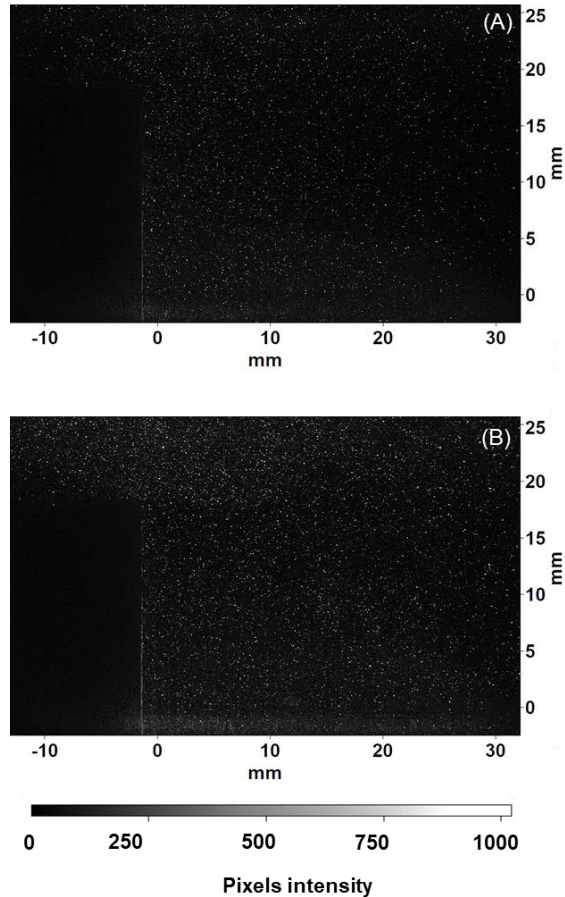


Fig. 2 Fluorescent particle image with (A) 0.75 g/L and (B) 2.0 g/L concentrations.

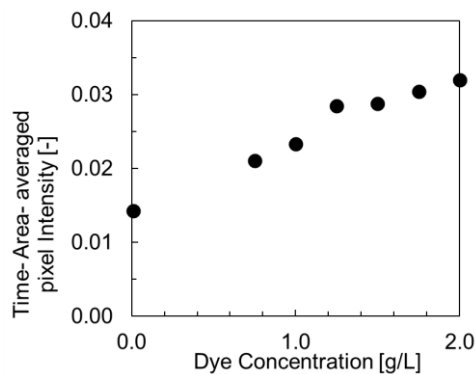


Fig. 3 Time- and area-averaged pixel intensities of fluorescent particle images at different dye concentrations.

A set of PIV experiments examining a flow over a turbine blade placed in the low-speed wind tunnel

were performed to assess the capability of the fluorescent particle in turbomachinery applications. Fig. 4 shows the test setup with the turbine blade manufactured in titanium alloy (Ti6Al4V) and previously tested under an engine representative test condition in a high-speed rotating turbine test facility (CT3) in the VKI. The blade and optics were set so that the laser sheet impinges on the blade suction side and the camera captures images on the blade-to-blade plane. The same seeding generator, laser system, camera, and objective lens previously mentioned were used for image capturing. Two optical filters, the 550 nm long-pass and the 532 nm band-stop were tested to evaluate the efficacy of the fluorescence light separation from the reflections. The dye concentration was set to 1.5 g/L. The aperture of the lens and laser pulse intensity were set to  $f/11$  and 9 mJ for the Mie scattering PIV case, whereas  $f/4$  and 22 mJ were used for the fluorescent PIV cases.

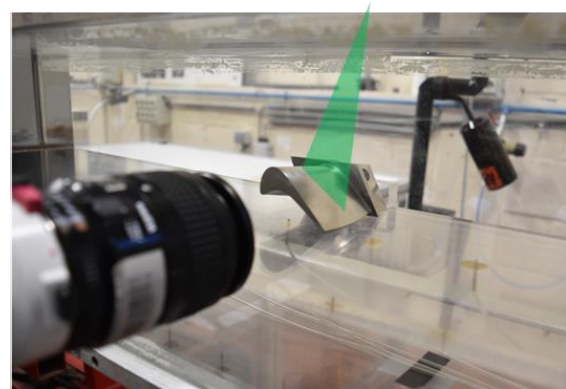


Fig. 4 Test setup for examination of a flow over the turbine blade.

Fig. 5 presents snapshots of (A) Mie scattering (B) fluorescent emission with 550 nm long-pass filter, and (C) fluorescent emission with 532 nm band-stop filter. In the Mie scattering image, a strong light reflection appears as a line on the blade suction surface and the blade hub endwall is evidently illuminated. Fluorescence cases show reduced reflections, especially with the band-stop filter. In such images, the minimum distance from the measurement point to the wall won't be limited by pixel saturation caused by reflections on the surface.

Fig. 6 shows instantaneous vector fields of three cases, with zoomed views and correlation maps of the interrogation windows indicated by red rectangles. The multi-pass cross-correlation method provided by *Davis 8.4* was used starting from 128-pixel initial square windows to 24-pixel final square windows. The window overlap was set to 50% for the last pass, resulting in a vector computation every approximately 0.5 mm. Computed vectors were validated through peak-to-peak ratio and median filter while no smoothing nor vector interpolation

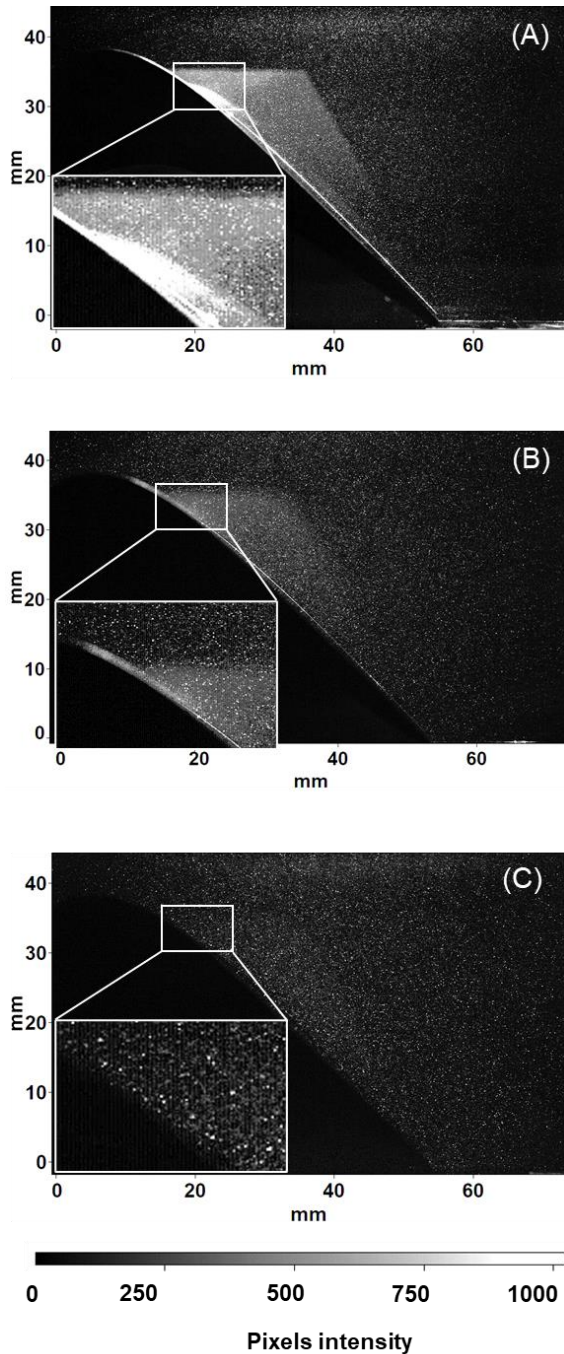


Fig. 5 Particle images capturing (A) Mie scattering, (B) Fluorescence with the low-pass filter, and (C) Fluorescence with the band-stop filter.

tools were activated. Close to the blade surface, the correlation map in the Mie scattering image is strongly affected by the reflection, thus the vector estimation at such location is questionable.

In the fluorescent PIV case, successful suppression of the reflection is achieved. Thanks to high optical density and narrow blocking band, the band-stop filter provides the cleanest raw particle image with almost invisible reflections, yielding a distinctive peak in the correlation map. Looking at vector fields close to the wall, the vector fields from fluorescent images show small vortex structures

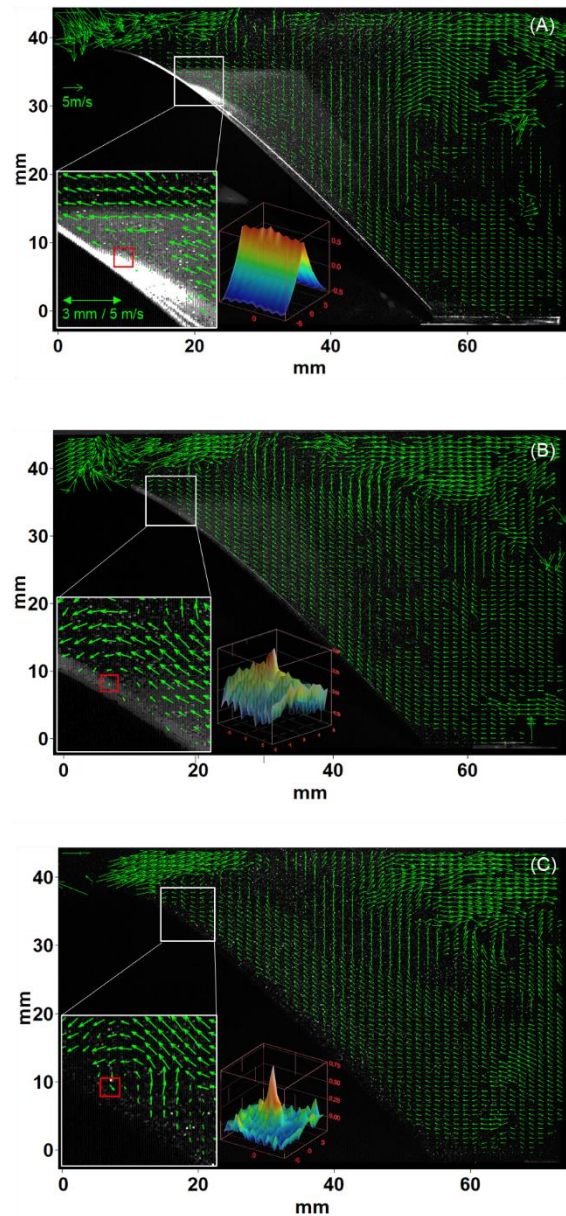


Fig. 6 Instantaneous vector fields and local correlation maps computed from (A) Mie scattering image, (B) fluorescent image with the low-pass filter, and (C) fluorescent image with the band-stop filter.

resolved with reasonable flow continuity along surroundings.

A statistical assessment of image quality is demonstrated by comparing the number of valid vectors at each interrogation window over 1500 instantaneous datasets as shown in Fig. 7. Prior to vector computation, mean background subtraction, moving window background subtraction, and particle intensity normalization were performed. Note that, the area at the top left corner of the field of view was poorly illuminated therefore vector estimation was often not successful. Overall, the fluorescent PIV with the band-stop filter provided a higher number of valid vectors by 5-10% compared to conventional Mie scattering PIV, conceivably thanks to the reduction of background noise

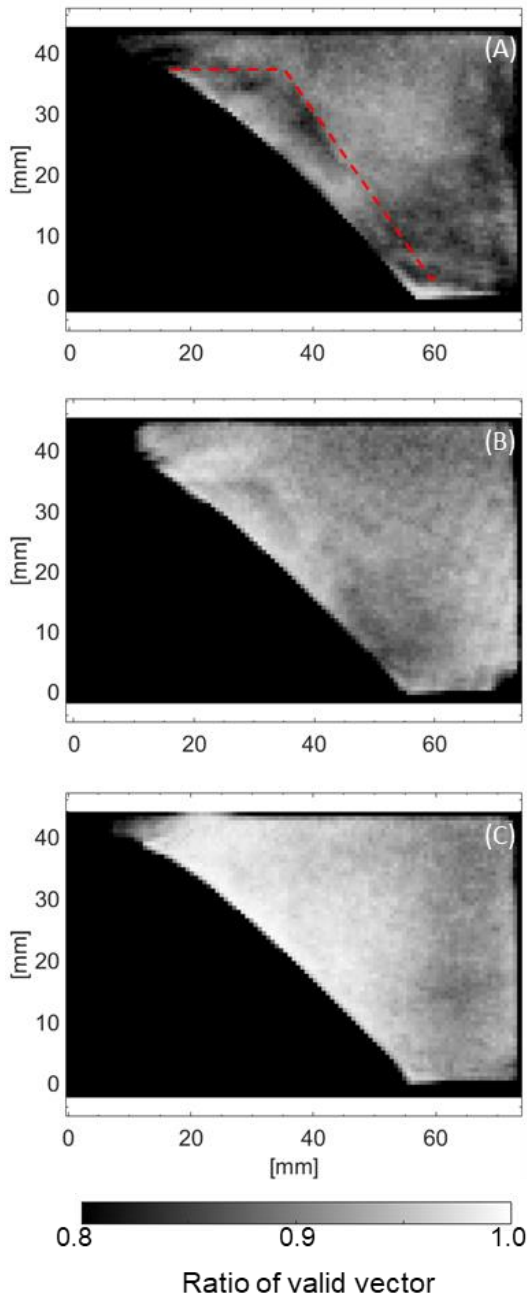


Fig. 7 Ratio of the number of valid vectors over 1500 datasets. (A) Mie scattering PIV, (B) fluorescent image with the low-pass filter, and (C) fluorescent image with the band-stop filter.

attributed to the reflections. In more detail, it is remarkable that vectors in the areas where there were reflections of the blade hub (indicated by red dotted line) were subject to be flagged as invalid in the Mie scattering case. Some vectors on the perimeter of blade hub image was most likely computed from image patterns consist of illuminated hub surface (high intensity) and empty background (low intensity). Such vectors should be discarded as they are not representing the flow, resulting in a fewer number of the available dataset in the location. Therefore, the minimization of background reflection in raw images is important. It

becomes more crucial in applications containing moving parts such as turbomachinery because background image subtraction is usually not applicable due to image-to-image variations. Under such circumstances, the advantage of the fluorescent PIV technique against reflection noise is further emphasized.

### EXPERIMENTAL FACILITY & TEST SETUP

The developed fluorescent tracer particles were tested in the rotating turbine rig of the VKI (Fig. 8). The principle of this short-duration turbine rig is the isentropic compression tube. The test rig allows high-pressure turbine (HPT) tests at engine representative conditions in terms of pressure ratio, Mach number, and Reynolds number. Rim seal purge flow is supplied from a pressure tank isolated from the compression tube. For this particular test campaign, the test rig was equipped with a single-stage HPT consisting of 34 vanes and 48 rotors, and the testing time was about 250 ms. The overview of the typical blow-down test sequence is shown in Fig. 9. The nominal flow condition relevant to the engine cruise condition was considered for the present test campaign (Table 1).

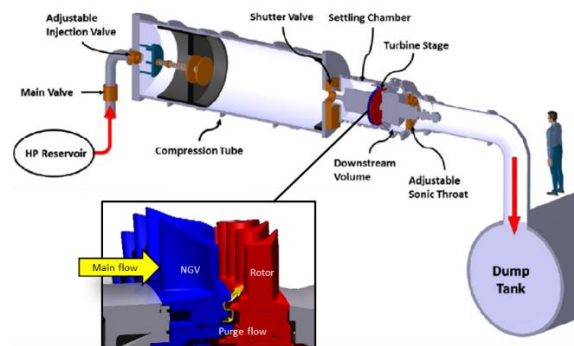


Fig. 8 High-speed short-duration rotating turbine test facility (CT3). Figure adopted from (6).

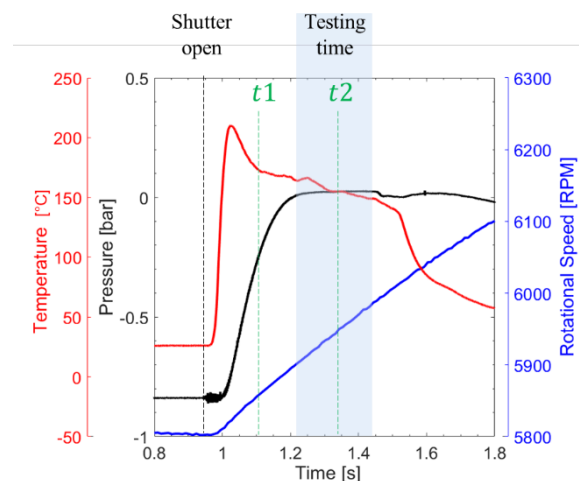


Fig. 9 A typical test sequence of the turbine test rig. Turbine inlet temperature (red), pressure (black), and rotational speed of the rotor disk (blue),

Table 1 Test condition of the turbine rig.

Parameter	Value	Units
$P_{01}$	1038	mbar
$T_{01}$	440	K
$P_{01}/P_{S3}$	2.2	-
$Re_{03}, C_{ax}$	$2.76 \cdot 10^5$	-
$Mach_{03,rel}$	0.78	-
$N_{rot}$	5920	RPM
$\dot{m}_{purge}$	1.74 % of $\dot{m}_{total}$	-

The meridional view of the test section is shown in Fig. 10. Plane 01 is located at half axial chord upstream of nozzle guide vane (NGV) leading edge and plane 03 is positioned at the downstream of the rotor, approximately 0.5 axial chord downstream of the rotor trailing edge. Pressure and temperature at plane 01 and 03 at midspan were measured by circumferentially distributed probes as well as hub endwall and shroud wall pressure taps, providing reference measurement values to monitor operating conditions. Additional slots at plane 01 and plane 03 were used to introduce seeding probes and a laser light sheet endoscope. The laser endoscope of 8 mm external diameter designed and built internally was inserted into the internal casing at the downstream of rotor stage, using a slot at plane 03. The scope yaw angle and radial position were adjusted by rotating the scope and changing the insertion depth. A high-speed Phantom v2012 camera and a high-speed Quantronix DarwinDuo dual cavity laser system were synchronized at 1 kHz acquisition frequency (laser output power: 20 - 25 W) by Stanford DG535 digital delay/pulse generators. The camera was equipped with a Nikon AF Micro-Nikkor 60mm  $f/2.8D$  lens and the 532 nm band-stop filter was attached to it for the fluorescent PIV test.

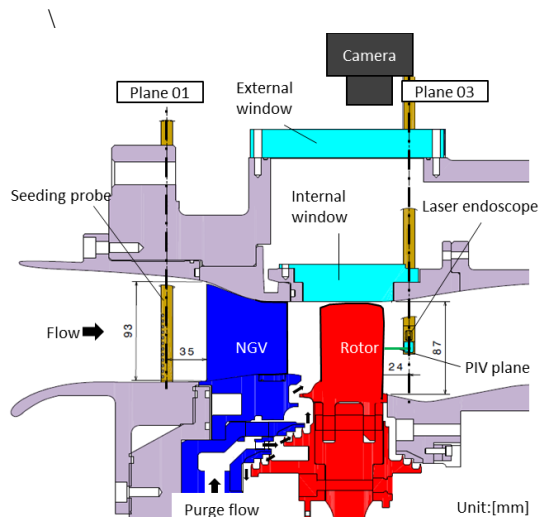


Fig. 10 Test section of CT3.

A complete illumination of the blade-to-blade planes in the rotor passage or at the rotor span higher than 58% was difficult due to the unoptimized access for the endoscope and highly turned rotor blade geometry. Besides, the curved surface of the window caused image distortion and its effect was further pronounced as the measurement plane approaches the hub. The light sheet illuminates not only particles but also other components on its traveling path, such as the casing surface and rotor blades, yielding significant background noise compared to Mie scattering light from particles. Therefore for Mie scattering PIV cases (no optical filter used), the rotor passage in which the most significant reflection appeared was covered with a black tape attached to the outer surface of the internal window to block the incidence of reflected light into the image sensor. Consequently, the region of interest was limited to a tangential plane near the rotor blade exit, located between 105 - 120% of rotor axial chord covering a full rotor pitch (0.78 vane pitch) at 50% rotor span as shown in Fig. 11. On the other hand, fluorescent PIV measurement did not require such treatment thanks to the cut-off of the incident of reflections by the optical filter. As a result, the field of view in the axial direction was extended to 60 - 120% of the rotor axial chord.

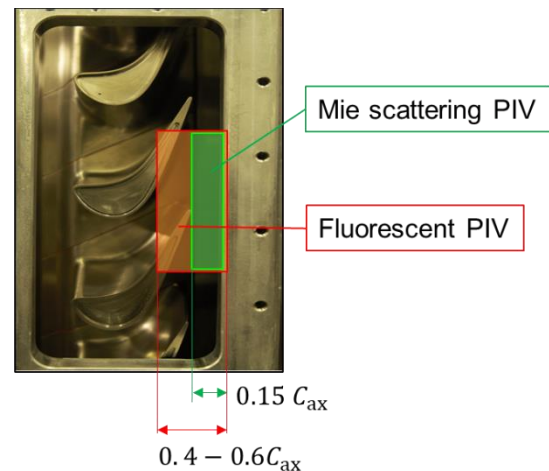


Fig. 11 Field of view of PIV measurements.

The fluorescent particles at 1.25 g/L concentration were seeded through three custom-made seeding probes installed upstream of the NGV row (plane 01) at different circumferential positions by reusing the insert slots originally designed for aero-thermal probes as shown in Fig. 12. In addition, the rim seal purge flow was seeded by injecting tracer droplets into the purge flow supply line. The total seeding mass flow rate injected through the seeding probes is estimated to be less than 0.2% of the main flow. The detailed test setup and processing method are described in [7].

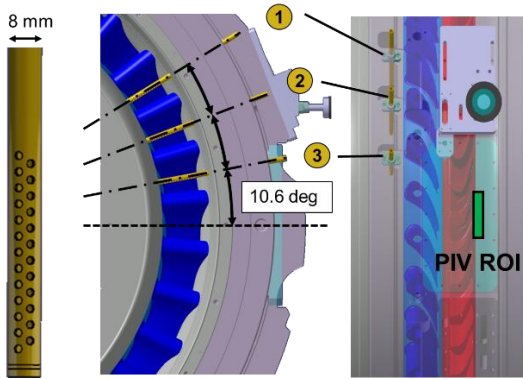


Fig. 12 Seeding setup in the turbine test rig.

## RESULTS

Fig. 13 (A) shows a cropped snapshot of a raw particle image taken without the optical filter. Reflections on the rotor surface and background are evident. Most notably, the reflection at the rotor trailing edge is excessively strong resulting in a residual image effect in the successive frame (pixels completely blacked out) which prevents the estimation of vectors in the region. Besides, the employment of pricey high-speed cameras should be avoided under such circumstances due to possible damage to the image sensor. The removal of the undesired reflection was achieved in the fluorescent particle images as shown in Fig. 13 (B) and (C) respectively taken at time instance  $t_1$  (when the flow is being established) and  $t_2$  (during testing time) as indicated in Fig. 9. A weak yet visible reflection on the rotor blade is assumed to be attributed to fluorescent oil accumulated on the blade surface. Fewer particles were observed in the image taken during the testing time. One of the possible causes is an accumulation of the oil droplets on the wet surface of the optical window absorbing fluorescent emissions from the particles. Besides, transient operation of the test rig in which the flow condition changes drastically while being established can also cause a deviation of seeding density from the optimum condition. The stator-rotor interaction flow may also prevent seeded flow from reaching certain areas as a function of relative stator-rotor positions, resulting in poorly seeded images at certain phases in certain regions.

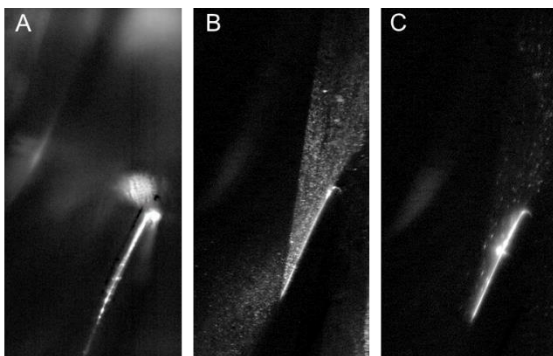


Fig. 13 Raw images in the rotor passage taken (A) without filter, (B), (C) with filter at  $t = t_1, t_2$ .

**Errore. L'origine riferimento non è stata trovata.** presents a comparison of absolute yaw angle in colormaps, subfigures (a), (b) show instantaneous plots at time instant  $t_1$  and  $t_2$ , whereas (c), (d) are phase-lock-averaged (PLA) results of fluorescent and Mie scattering PIV performed in single blow-down test, and (e) is obtained from steady-state RANS simulation. The fluorescent PIV-PLA was calculated by combining the datasets taken before and during the testing time to increase the number of raw images. In total 250 and 229 datasets were applicable for Mie scattering and fluorescent PIV-PLA. The PLA method and the simulation setup are described in [7] and [8], respectively. Fig. 14 shows yaw angle profiles extracted from **Errore. L'origine riferimento non è stata trovata.** (c)-(e) along with the dotted lines  $L_1$  and  $L_2$ . While  $L_1$  goes through the rotor passage with an angle approximately aligned to the exiting flow,  $L_2$  is defined at constant axial location  $x/C_{ax} = 1.1$ . In the same manner, Fig. 16 and Fig. 17 respectively present colormaps and profiles of velocity magnitude relative to the rotor.

The area of colormap illustrates the extended measured area by fluorescent PIV compared to Mie scattering PIV. Vectors in the rotor passage and proximity to the blade surface were partially retrieved, especially at  $t = t_1$  when more particles appeared in the raw images as seen in Fig. 13. However, since the flow is still being established at  $t_1$ , the flow regime deviates from the nominal steady condition, the rotor wake leans more towards downstream. On the contrary, at  $t = t_2$ , i.e. during testing time, the flow field shows a fairly similar structure to Mie scattering PIV-PLA and RANS even though it has a notable amount of blank spots due to the lack of particles in the image.

In terms of the profiles, comparisons along  $L_1$  show good agreement, indicating fluorescent PIV is capable of capturing accelerating flow through the rotor passage. On the other hand, the comparison along  $L_2$  shows diversified profiles. The Mie scattering PIV-PLA presents a similar trend predicted by RANS with approximate offsets of 10 degrees and 15 m/s. The fluorescent PLA shows a discrepancy corresponding to 0.1 to 0.2 rotor pitch in the location of the rotor wake which is signified by the local maximum of yaw angle and the local minimum of velocity magnitude. This is due to the PLA processing including the dataset taken before the testing time. Acquiring more images by repeating blow-down tests or increasing acquisition frequency is a solution to obtain testing-time-only PLA results and reach well-converged flow fields. Besides, with the current setup, the valid number of the vectors has inhomogeneous distribution as shown in Fig. 18. Thus, another future perspective of the technique is an improvement of illumination setup to enlarge the measurement area and optimization of the seeding method to acquire high-

quality particle images during transient test operation.

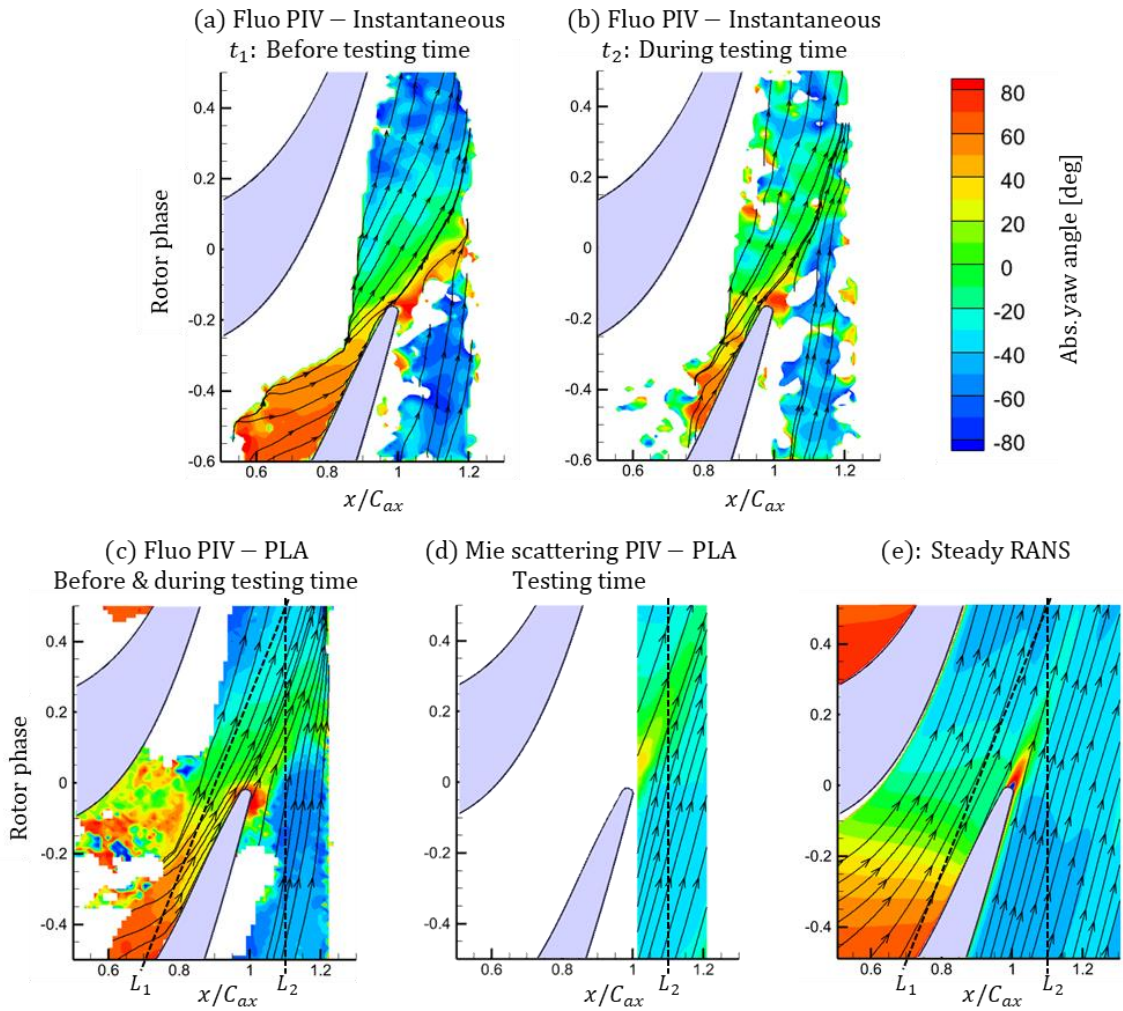


Fig. 14 Comparison of yaw angle obtained from fluorescent PIV, Mie scattering PIV, and steady-RANS simulation.

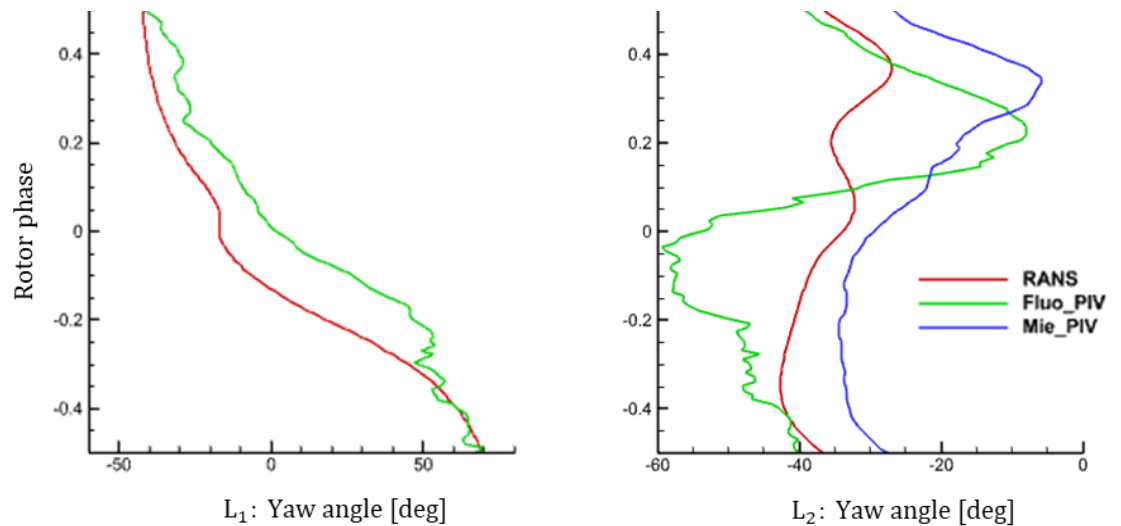


Fig. 15 Profiles of yaw angle extracted along  $L_1$  and  $L_2$ .



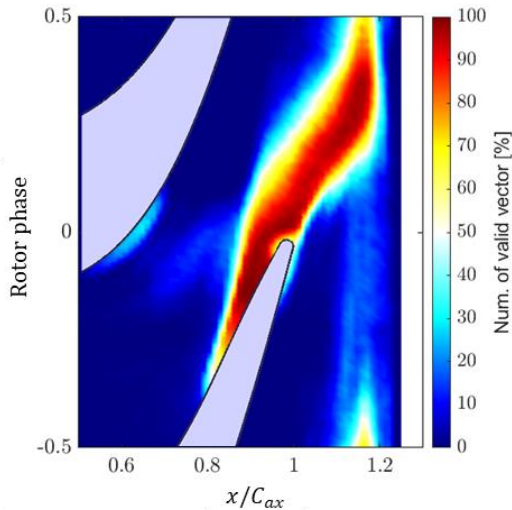


Fig. 18 Valid number of vectors used for fluorescent PIV-PLA.

## CONCLUSION

P567 dye-doped sub-micron scale droplets have been investigated for PIV measurements in turbomachinery flows. The fluorescence intensity in a form of sub-micron scale droplets was investigated by counting pixel intensity of particle images, the intensity level was found to be principally proportional to the dye concentration.

PIV tests in the low-speed wind tunnel with the metallic turbine blade and the laser sheet oriented to impinge the blade surface were performed to assess the effectiveness of the fluorescent tracer particles and optical filters. The combination of the fluorescent tracer and the band-stop optical filter successfully removed undesired reflections and enabled the acquisition of reasonable vector fields throughout the illuminated area including the close proximity to the highly reflective surfaces.

The fluorescent PIV technique was applied in the high-speed short-duration rotating turbine rig that simulates engine representative test conditions. The acquisition of the flow field in the rotor passage and in proximity to the blade surface was achieved. During testing time, low seeding density was found in the images resulting in fewer valid vectors. The quantitative comparison of yaw angle and velocity magnitude among fluorescent PIV, Mie scattering PIV, and steady RANS results presented a good agreement in the rotor passage while diversified results at downstream of the rotor. Overall, the developed fluorescent tracer technique demonstrated the capability of reflection removal in the turbomachinery test rig, the potential will be further exploited by improved illumination and seeding setups which will lead to an increased number of applicable images for processing.

## ACKNOWLEDGMENTS

The authors would like to acknowledge the Yoshida Scholarship Foundation for support of this study.

## REFERENCES

- [1] Lee, J., & Nishida, K. (2003). Simultaneous flow field measurement of DI gasoline spray and entrained ambient air by LIF-PIV technique (No. 2003-01-1115). SAE Technical Paper.
- [2] Kosiwczuk, W., Cessou, A., Trinite, M., & Lecordier, B. (2005). Simultaneous velocity field measurements in two-phase flows for turbulent mixing of sprays by means of two-phase PIV. *Experiments in fluids*, 39(5), 895-908.
- [3] Chennaoui, M., Angarita-Jaimes, D., Ormsby, M. P., Angarita-Jaimes, N., McGhee, E., Towers, C. E., ... & Towers, D. P. (2008). Optimization and evaluation of fluorescent tracers for flare removal in gas-phase particle image velocimetry. *Measurement Science and Technology*, 19(11), 115403.
- [4] Petrosky, B. J. (2015). Particle Image Velocimetry Applications of Fluorescent Dye-Doped Particles (Doctoral dissertation, Virginia Tech).
- [5] Bhattacharya, S., Berdanier, R. A., Vlachos, P. P., & Key, N. L. (2016). A new particle image velocimetry technique for turbomachinery applications. *Journal of Turbomachinery*, 138(12), 124501.
- [6] Andreoli, V., Lavagnoli, S., Paniagua, G., & Villace, V. F. (2016). Robust model of a transient wind tunnel for off-design aerothermal testing of turbomachinery. *Measurement*, 82, 323-333.
- [7] Okada, M., Pinho, J., Cernat, B., & Lavagnoli, S. (2022). Particle image velocimetry in a high-speed short-duration turbine test rig. *ASME TurboExpo2022*. GT2022-81271.
- [8] Cernat, B., Pinho, J., Okada, M., & Lavagnoli, S. (2022). Experimental Investigation of a High-Speed Turbine with Rainbow Rotor and Rim Seal Purge Flow. *ASME TurboExpo2022*. GT2022-83129.